Parametrization of a reactive many-body potential for Mo–S systems

Tao Liang, Simon R. Phillpot, and Susan B. Sinnott*
Department of Materials Science and Engineering, University of Florida, Gainesville, Florida 32611, USA
(Received 27 January 2009; revised manuscript received 5 May 2009; published 8 June 2009)

We present an interatomic potential for the Mo-S system based on the second-generation reactive empirical bond-order formalism. An analytic function is introduced to the bond-order term to capture the effect of the coordination number on the binding energy. The fitting scheme used for this potential is optimized by appropriate selection of the functions, training databases, initial guesses, and weights on each residual—the four factors that are involved in a weighted nonlinear least-squares fitting. The resulting potential is able to yield good agreement with the structure and energetics of Mo molecules, two-dimensional Mo structures, three-dimensional Mo crystals, small S molecules, and binary Mo-S crystal structures. We illustrate the capabilities of the new potential by presenting results of the simulation of friction between MoS_2 layers. The results are consistent with our previous static potential surface calculations using density-functional theory.

DOI: 10.1103/PhysRevB.79.245110 PACS number(s): 31.15.xv, 34.20.Cf, 34.20.Gj, 46.55.+d

I. INTRODUCTION AND BACKGROUND

Molybdenum disulphide (MoS_2) is widely used as a solid lubricant, as a hydrodesulfurization catalyst, and as a material for electronic devices.[1,2] Unsurprisingly, therefore, it has attracted considerable attention in the simulation community. A number of first-principles electronic-structure calculations have been performed to characterize the structural,[1,3–5] electronic,[1,5–9] tribological,[7,10–13] and catalytic properties[1,3,5,14–20] of MoS_2. Quantum mechanics based first-principles calculations are, however, less able to simulate dynamic and kinetic problems, such as tribological sliding, than molecular dynamic (MD) methods using empirical potentials. Nevertheless, very few molecular dynamic simulations have been performed on MoS_2 since no many-body empirical potential for Mo-S systems has yet been developed. In this paper we introduce a reactive many-body interatomic potential for the Mo-S system. We anticipate that a reactive potential for use in MD simulations will lead to powerful insights into the tribological properties of MoS_2.

The framework we adopt for this Mo-S potential is similar to that used for the reactive empirical bond-order (REBO) (Refs. 21 and 22) potential, which has proved so successful for carbon-based systems. We find that this potential is able to yield good agreement with the structure and energetics of Mo molecules, two-dimensional (2D) Mo structures, three-dimensional (3D) Mo crystals, small S molecules, and Mo-S binary crystal structures.

Abell-Tersoff[23–27] and REBO potentials introduce a parametrized bond-order function into a pair potential to describe the many-body effects and chemical bonding of a given system. The bond-order function allows these potentials to use the same parameters to describe several different bonding states associated with a system. Thus, at least to some extent, the potential is able to characterize chemical reactions correctly. The analytic forms for the bond-order term in the original Tersoff potentials were first parametrized to group IV elements such as carbon, silicon, germanium, and their compounds. For example, the Tersoff potential for Si was parametrized to a number of properties of diatomic and solid-state structures including their energetics, elastic properties, and vacancy formation energy. By recognizing that the Tersoff empirical bond-order scheme is also capable of describing bonding in molecular single-component systems such as hydrogen and oxygen, Brenner[21] developed the REBO potential for hydrocarbon systems where single, double, and triple bonds, as well as radicals and conjugated bonds, were correctly treated, and the subsequent second-generation formalism[22] improved its performance. Though it does not treat electrons explicitly or include any quantum effects, the REBO potential has proved that it can nearly always be qualitatively predictive and often quantitatively accurate. Moreover, it is able to model large systems (many millions of atoms) on standard workstations for relatively long times (several nanoseconds), which would be computationally impossible for more accurate first-principles approaches.

Unlike other empirical potentials, the REBO potential allows for bond breaking and bond formation to occur over the course of a simulation. There is also an updated parametrization: the adaptive intermolecular reactive empirical bond order (AIREBO),[28] which adds another level of refinement albeit at a computational cost. In 2004, the second-generation REBO was extended to both CHF (Ref. 29) and CHO (Ref. 30) systems.

Importantly, for the Mo-S system, Brenner[31] showed that the Tersoff-based approach is fundamentally the same as the embedded-atom method (EAM) (Refs. 32 and 33) approach, which is widely used to describe metallic bonding. Indeed, we have successfully parametrized a many-body potential based on the Tersoff formalism to describe face-centered-cubic (fcc) Cu.[34]

Here, building on the proven framework of the REBO potential, we develop a many-body Mo-S potential energy expression that primarily focuses on the structural and elastic properties of MoS_2 while maintaining its transferability to other systems such as pure Mo structures, low coordinated S structures, and some other binary structures.

In Sec. II the analytic formalism of this many-body Mo-S potential is presented. This is followed by an overview of the fitting scheme used for the parametrization. Within the fitting framework, the paper gives the fitting results of pairwise parameters in Secs. II C–II E. To separate the coordination

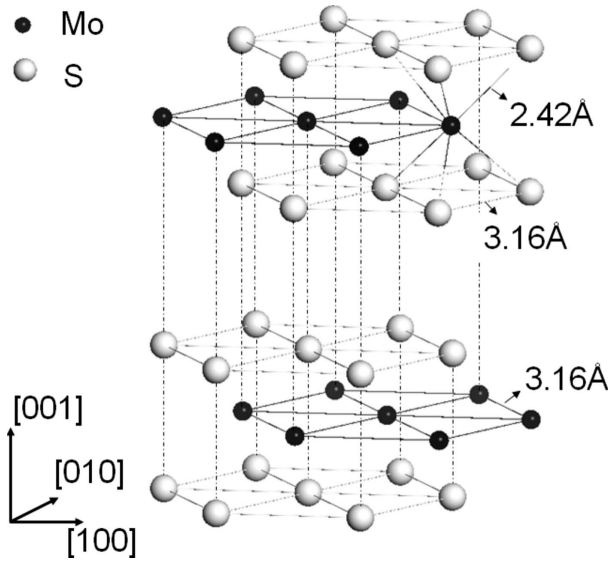

FIG. 1. Crystal structure of MoS_2.

contribution from the angular contribution to many-body effects, a coordination function is introduced to the bond-order term in the Mo-S potential. This coordination function reflects the change in the binding energy as a function of bond density in a manner similar to that used in the EAM (Refs. 32 and 33) approach. The parameters in the Lennard-Jones[35,36] potential are also given to characterize the van der Waals (vdW) interaction between the S-Mo-S trilayers. Section III demonstrates the capabilities of the newly developed many-body Mo-S potential for the case of nanotribology of sliding MoS_2/MoS_2 surfaces.

II. MANY-BODY MOLYBDENUM-SULFUR POTENTIAL

MoS_2 has a lamellar crystal structure formed by stacking S-Mo-S trilayers (Fig. 1). Each Mo atom lies at the center of the triangular prism formed by its six neighboring S atoms, thereby forming a MoS_6 unit. The bonding in each S-Mo-S trilayer is mainly covalent in nature and thus strong. By contrast, the S-Mo-S trilayers are weakly bonded to each other by vdW forces.

A. Analytic form of the Mo-S potential

The Mo-S many-body empirical potential has the form

$$E_b = \frac{1}{2}\sum_{i\neq j} f_{ij}^C(r_{ij})[V^R(r_{ij}) - b_{ij}V^A(r_{ij})]$$

$$= \frac{1}{2}\sum_{i\neq j} f_{ij}^C(r_{ij})\left[\left(1+\frac{Q}{r_{ij}}\right)A\cdot e^{-\alpha\cdot r_{ij}} - b_{ij}B\cdot e^{-\beta\cdot r_{ij}}\right], \quad (1)$$

where E_b is the binding energy of a system and r_{ij} is the interatomic separation between atoms i and j. $V^R(r_{ij})$ and $V^A(r_{ij})$ in Eq. (1) are the pairwise repulsion and attraction, respectively. In addition, $f_{ij}^C(r_{ij})$ is the cutoff function and b_{ij} is the bond-order term. Thus, the first part of Eq. (1) establishes that the pair interaction between an atom i and a neighbor j depends on the distance between the two atoms, but the strength of this bond is modified by the bond-order term, b. The bond-order term can be regarded as a measure of bond strength, which is determined by the many-body interactions of the environment on atom i. Thus, this formula allows the use of the same pairwise parameters to characterize the different bonding states of a system. The first part of Eq. (1) is the master formula underlying the Abell,[23] Tersoff,[24–27] and REBO (Ref. 22) potentials, which was first introduced by Abell.[23] In his original paper, Abell[23] argued that the coordination number is the dominant topological variable in the determination of the bond order and thus the binding energy. Generally, the bond-order value decays quickly with increasing coordination number and saturates at high coordination number.

The pairwise repulsion $V^R(r_{ij})$ in Eq. (1) is identical to that in the second-generation REBO (Ref. 22) potential. In particular, unlike the Abell and Tersoff potentials, this potential follows REBO by including a Q/r_{ij} term in $V^R(r_{ij})$, which can adjust the stiffness of the repulsion. The single exponential decay term in the attractive term, $V^A(r_{ij})$, is the same as in the original Tersoff potential and simpler than the sum of exponentials in REBO. The cutoff function, $f_{ij}^C(r_{ij})$, is the same as in Tersoff and REBO; it is described below. The Q, A, α, B, and β in Eq. (1) are pairwise parameters. Since each type of bond (Mo-Mo, S-S, and Mo-S) has one set of pairwise parameters, there are three sets of pairwise parameters associated with this potential.

The bond order, b_{ij}, in Eq. (1) consists of two many-body terms: the bond angle term, G, and the coordination term, P,

$$b_{ij} = \left[1 + \sum_{k\neq i,j} f_{ik}^C(r_{ik})\cdot G[\cos(\theta_{ijk})] + P(N_i)\right]^{-1/2}. \quad (2)$$

$P(N_i)$ is given as

$$P(N_i) = -a_0\cdot(N_i - 1) - a_1\cdot e^{-a_2\cdot N_i} + a_3, \quad (3)$$

where a_0-a_3 are parameters and N_i is the number of neighbors of atom i, independent of their type, i.e.,

$$N_i = N_i^{\mathrm{Mo}} + N_i^{\mathrm{S}}, \quad (4a)$$

where

$$N_i^{\mathrm{Mo}} = \sum_{k\neq i,j}^{\mathrm{Mo}} f_{ik}^C(r_{ik}) \quad (4b)$$

and

$$N_i^{\mathrm{S}} = \sum_{l\neq i,j}^{\mathrm{S}} f_{il}^C(r_{il}), \quad (4c)$$

where $f_{ik}^C(r_{ik})$ and $f_{il}^C(r_{il})$ are the cutoff functions. Their form is identical to that of the Tersoff and REBO potentials and is given by

$$f_{lk}^{C}(r_{ij}) = \begin{cases} 1 & r_{ij} < R_{lk}^{\min} \\ \{1 + \cos[(r_{ij} - R_{lk}^{\min})\pi/(R_{lk}^{\max} - R_{lk}^{\min})]\}/2 & R_{lk}^{\min} < r_{ij} < R_{lk}^{\max} \\ 0 & r_{ij} > R_{lk}^{\max}. \end{cases} \quad (5)$$

$P(N_i)$ is a newly introduced function to this potential to separate the coordination term from the bond angle term. It is constructed based on the relationship between a summation of both the angular term and the coordination term (M_{tot}) and coordination number (N_i), where M_{tot} is defined as

$$M_{\text{tot}} = \left(\frac{1}{b_{ij}}\right)^2 - 1 = \sum_{k \neq i,j} f_{ik}^{C}(r_{ik}) \cdot G[\cos(\theta_{ijk})] + P(N_i). \quad (6)$$

Assuming the mean value of $G[\cos(\theta_{ijk})]$ is a_0 in Eq. (3), M_{tot} thereafter can be expressed alternatively in terms of a_1, a_2, and a_3,

$$M_{\text{tot}} = -a_1 \cdot e^{-a_2 \cdot N_i} + a_3. \quad (7)$$

The θ_{ijk} in Eqs. (2) and (6) is the angle between bonds ij and ik. $G[\cos(\theta_{ijk})]$ has the same form as for the hydrocarbon REBO potential,[22] which is a sixth-order polynomial,

$$G(x) = b_0 + b_1 x + b_2 x^2 + b_3 x^3 + b_4 x^4 + b_5 x^5 + b_6 x^6, \quad (8)$$

in which b_0–b_6 are parameters that are fitted. The choice of this selection for $G[\cos(\theta_{ijk})]$ is justified in Sec. II F. The many-body parameters, i.e., parameters in $G[\cos(\theta_{ijk})]$ and $P(N_i)$, are functions only of the element type, i, and are independent of the bond type. Thus there are only two sets of many-body parameters in this Mo-S potential, one for Mo and one for S.

The cutoff function in Eq. (5) gradually reduces the interactions to zero over the range $R_{ij}^{\min}$ to $R_{ij}^{\max}$. However, this artificial termination of interactions is not without problems. In particular, an unrealistically large force is generated for interatomic distances in this range. So as to minimize the effect for any given bond length, it is best to maximize the separation between $R_{ij}^{\min}$ and $R_{ij}^{\max}$. It is also important to make an appropriate choice of the cutoff radius in this Mo-S potential. The bond length of Mo in body centered cubic (bcc), the stable structure in nature, is 2.73 Å, with the second-neighbor distance being 3.16 Å. It is essentially impractical and extremely undesirable to set the cutoff radius such that only the first nearest neighbors of the bcc structure are considered. Thus, the cutoff for Mo-Mo bonds is set at $R_{\text{Mo}}^{\min}$=3.5 Å, which is beyond the second-neighbor distance and allows about 11% strain in the bcc structure before it reaches $R_{\text{Mo}}^{\min}$. The exponential decay of the binding energy with interatomic separation, as shown in Eq. (1), makes the contributions to the energy from third neighbors and beyond very small. As is well known, the structure of S at 300 K and 1 atm consists of an eight-membered ring, in which the first-neighbor distance is 2.04 Å and second-neighbor distance is 3.06 Å. Thus, it is reasonable to set $R_{\text{S}}^{\min}$ such that only first nearest neighbors in sulfur will be considered. Generally speaking, the second nearest Mo-S bonds in any of Mo-S binary structures (metal sulfides) are much larger than the first-nearest-neighbor Mo-S bonds. For example, the first nearest Mo-S bond length in MoS_2 is 2.42 Å (see Fig. 1), whereas the second nearest Mo-S bond length is 4.56 Å, which makes their contribution to the energy of the system negligible. The cutoff radius of Mo-S bonds thus is set so as to include first-nearest-neighbor interactions only.

With the choice of cutoff, Mo-Mo interactions would be included in the MoS_2 structure for which the Mo-Mo bond distance is 3.16 Å (see Fig. 1). Physically, the short-ranged bonds in MoS_2 have both ionic and covalent characters. Therefore Mo atoms in MoS_2 are partially positively charged with a shorter effective atomic radius than they have in the neutral state. That is to say, the equilibrium Mo-Mo bond length within MoS_2 when they are in a positively charged state is shorter than when they are in a neutral state. As a result, the predicted bond energy as well as bond length of the Mo-Mo bond in some binary structures will be overestimated based on this charge-free formalism. We compensate for the charge-free form of the potential by penalizing the binding energies of some structures that do not exist in nature in the parametrization process (Sec. II B). Nevertheless, as we shall see the final fitted potential is still able to describe the properties of the following structures relatively well: Mo molecules, two-dimensional Mo structures, three-dimensional Mo crystals, small S molecules, such as S_2 and S_3, and Mo-S binary crystal structures except the hypothetical ZnS and CsCl structures.

B. Overview of the fitting scheme

The database used for parametrization of the Mo-S potential is obtained from density-functional theory (DFT) calculations. However, given the general concern of using conventional DFT to describe vdW forces in layered structures,[37,38] two vdW-related parameters of MoS_2 are fit to experimental values for the lattice parameter c and elastic constant c_{33}. All of the DFT calculations are performed with the plane-wave density-functional theory software code Vienna *Ab initio* Simulation Package (VASP) (Refs. 39–43) using the generalized gradient approximation (GGA) (Refs. 44–46) pseudopotentials with the core electron correction for Mo. The energy cutoff is 600 eV. Though it tends to underestimate the binding energy and give larger lattice constants,[1] the GGAs of Perdew and Wang[46] have been widely used in solid-state applications and have been proved to be quite successful in predicting relative energetics, elastic properties, and lattice constants of different phases. It is therefore used in this work.

Fitting the many-body Mo-S potential consists of three steps: (1) conducting DFT calculations to obtain the data-

bases that are used for the fitting; (2) fitting the pairwise parameters and bond-order values of different structures; and (3) fitting the many-body parameters by treating the pairwise parameters from the second step as known parameters. In the first step, a range of structures with different bonding environments, including molecules, 2D lattices, and 3D crystals, is considered. For each structure, the internal energy vs unit volume (lattice parameter for 2D structures and bond length for molecules) has been calculated using DFT by homogeneously expanding and shrinking the structure. Within the nearest-neighbor approximation, the resulting energy per bond E_{bond} near the bond energy minimum (no more than $\pm 1\%$ strain of equilibrium bond length of each structure) is fit to a simple parabolic function of the bond length, r,

$$E_{\text{bond}}(r) = c_0 + c_1 r + c_2 r^2, \tag{9}$$

where c_0, c_1, and c_2 are parameters. The equilibrium bond length ($\frac{-c_1}{2c_2}$), bond energy, and bond stiffness (the second derivative of the bond energy over the bond length at the equilibrium state, i.e., $2c_2$) can be obtained from Eq. (9). As discussed above, there are three types of bonds in this Mo-S system. The databases (bond energy or atomization energy, bond length, and bond stiffness of different structures) obtained from Eq. (9) are categorized to Mo-Mo, S-S, and Mo-S databases and presented in Secs. II C–II E, respectively. These three databases are the main training set for both pairwise parameter and many-body parameter fittings. In addition to these databases, two more important properties of MoS_2 are calculated using DFT and are considered only in the parametrization process of many-body terms: the energy of the stacking fault on the basal plane S (0001) in a single S-Mo-S trilayer and the elastic constants c_{11} and c_{33} of a single S-Mo-S trilayer. The details of these two properties are given in Sec. II F.

The fitting algorithm used for the second and third steps is a weighted nonlinear least-squares method (LSM) with the Levenberg-Marquardt (LM) (Refs. 47 and 48) minimization. The fitting algorithm requires a model or function(s) that relates the response data to the predictor data with one or more unknown coefficients (parameters). The algorithm starts from the initial guesses for the potential parameters and, based on the functional forms and the fitting data, computes the summation of the weighted square of residuals. The summed squared residual is then minimized by the LM iteration method. Finally, the fitting returns the optimized potential parameters and the value of the squared two norms of the residual (residual norm). To minimize the arbitrariness of the results that may be introduced by the choice of initial guesses, the whole process is iterated using the returned parameters from previous fitting as initial guesses for the next fitting iteration step. The residual norm is used to evaluate the quality of the model and/or functions: the smaller the residual norm is, the better the functions reproduce the data used for the fitting. Thus, the residual norm is dependent on four factors involved in this LSM-LM fitting algorithm: function(s), database(s), initial guesses, and weights on each residual. In addition to iterating during the LSM-LM fitting, a number of strategies to optimize the selection of these four factors are also used in the following parametrization process of pairwise and many-body parameters.

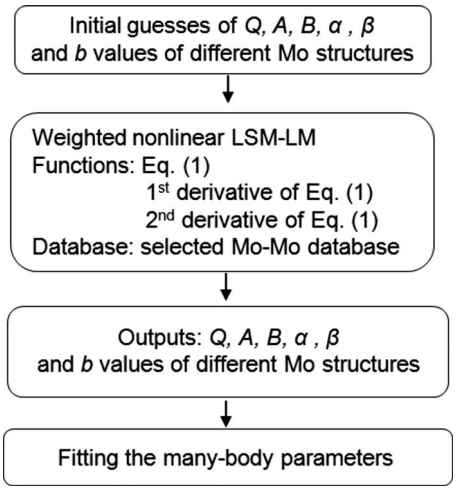

FIG. 2. Flow chart of the process for fitting the pairwise parameters for Mo bonds.

In the second step, the pairwise parameters (A, Q, B, α, and β) in Eq. (1) and discrete bond-order values of different structures of different bond types (Mo-Mo, S-S, and Mo-S) are fit to the corresponding Mo-Mo, S-S, and Mo-S databases, respectively. Using Mo bonds as an example, a flow chart of the fitting of pairwise parameters is given in Fig. 2. The energy per atom or atomization energy in the database is associated with the bond energy in Eq. (1). The bond length and bond stiffness in the Mo-Mo database are associated with the first and second derivatives of the binding energy [Eq. (1)], respectively. Thus the model or functions used for the present LSM-LM fitting (Fig. 2) contain Eq. (1) and its first and second derivatives. We equally weigh these three properties of the bond. Within each property (atomization energy/energy per atom, bond length, and bond stiffness), the weight of different structures is chosen to be proportional to the binding energy per atom of each structure. Thus the more stable structures (i.e., those with the largest negative energies) will be more heavily weighted in the LSM-LM fitting. This weighing strategy is applied to all of the LSM-LM fitting procedures used in this paper. It is worthwhile to note that not all the data points are used in this parametrization process. For example, the bond stiffness values of the Mo molecules are excluded because they are less relevant to the systems of interest here and because fitting to them decreases the accuracy of other more relevant properties. The bcc structure of Mo is of particular interest because it is the stable bulk phase. Because the ratio of the second- to first-neighbor distance in bcc is only 1.15 (the first eight neighbors are at 0.866 of the bcc lattice constant, with the 6 s neighbors at one lattice constant), it is not appropriate to consider just the first nearest neighbors, which is the assumption of present fitting scheme. Thus the data points from the bcc structure of Mo bonding are intentionally excluded. The same parametrization process has been applied to S-S and Mo-S systems. The results of the pairwise parameter fitting for Mo-Mo, S-S, and Mo-S bonds are given in Secs. II C–II E, respectively.

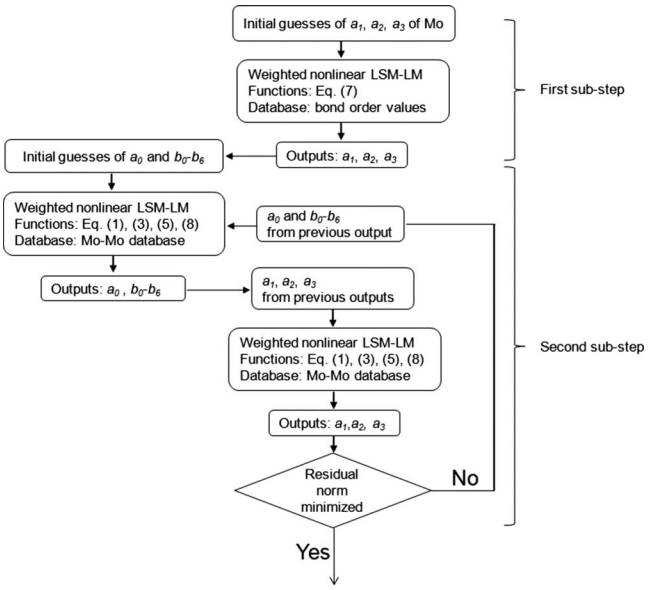

FIG. 3. Flow chart of first two substeps of parametrization of the many-body parameters for Mo.

As discussed in Sec. II A, there are two sets of many-body parameters in this binary system, one for Mo and one for S. For each parameter set, there are 11 unknown many-body parameters (a_0–a_3 and b_0–b_6). The parametrization process in the third step contains three substeps: (1) fitting the a_1, a_2, and a_3 based on bond-order values obtained from the pairwise fitting; (2) iterating the weighted nonlinear LSM-LM fitting on a_0 and b_0–b_6 and on a_1, a_2, and a_3 alternately using the Mo-Mo and S-S databases for the corresponding Mo and S many-body parameters, respectively; and (3) an overall consideration on both Mo many-body parameters and S many-body parameters using all the databases (Mo-Mo, S-S, and Mo-S databases and two properties of S-Mo-S single trilayer) except those excluded for the reasons described above. The flow charts of the first two substeps and the third substep are given in Figs. 3 and 4, respectively.

To reduce the number of parameters to be fit, we start the third step by fitting a_1, a_2, and a_3 in Eq. (7) to M_{tot} values as shown in Fig. 3. As suggested in Eqs. (3), (6), and (7), M_{tot} is independent of a_0, which is assumed to be the mean value of $G[\cos(\theta_{ijk})]$. The M_{tot} values can be directly calculated from discrete bond-order values of different Mo structures [Eq. (6)], which are obtained from the pairwise parameter fitting. The returned a_1, a_2, and a_3 are then considered as known parameters for the next step of fitting parameters a_0 and b_0–b_6, where the residual is computed based on the Mo-Mo database and Eq. (1), in which the bond-order value is calculated based on Eqs. (3), (5), and (8). The way to compute Eq. (1) here is not limited to first nearest neighbors. Thus the bcc phase of Mo is included in the training set from the second substep onward. The outputs of a_0 and b_0–b_6 are then used as known parameters to compute the bond-order value in the next LSM-LM fitting of a_1, a_2, and a_3. The initial guesses of a_1, a_2, and a_3 for this step of fitting are the outputs from first substep. The outputs will again be regarded as the known parameters for the iteration of fitting on a_0 and b_0–b_6. We repeat this weighted nonlinear LSM-LM fitting until the residual norm is minimized. The same fitting processes are applied to the S atoms.

Ideally, the many-body parameters obtained from fitting to the pure systems would be directly transferable to binary structures. However, as discussed at the end of Sec. II A, this charge-free formalism fails to describe some bond properties in some binary structures. Since the primary focus of this study is the tribological properties of MoS_2, the highly coordinated S structures and some binary structures, in particular the CsCl and ZnS structures, are not used in the third substep. As shown in Fig. 4, an iteration of two fitting processes, one process for Mo many-body parameters and the other for S many-body parameters, is used to optimize the overall fitting results. For the first iteration run, we use the output parameters from the second substep as input guesses for the fitting process. The fitting results provide better estimates of those parameters for the next iteration step. When the fitting process is applied to the Mo many-body parameters, the S many-body parameters from previous outputs are considered as known parameters. In turn, the many-body parameters for

TABLE I. DFT calculated database used in fitting scheme for Mo-Mo bonds.

Structures	Coordination number	Bond length (Å)	Energy per atom (eV)	Energy per bond (eV)	Bond stiffness (eV/Å^2)
Dimer	1	1.95	−6.41	−12.82	55.5[a]
Trimer	2	2.24	−6.53	−6.53	26.1[a]
Hexagonal	3	2.35	−7.78	−5.19	15.3
Square	4	2.47	−8.25	−4.13	12.4
Diamond	4	2.49	−8.61	−4.31	11.8
Triangle	6	2.61	−8.41	−2.80	6.9
sc	6	2.62	−9.58	−3.19	9.2
bcc[b]	8/14[c]	2.75[a](2.73[b])	−10.80[a]	−2.70[a]	8.0[a]
fcc	12	2.84	−10.38	−1.73	4.8

[a]Not used in the fitting process of pairwise parameters.
[b]Experimental value.
[c]8 is for first-nearest-neighbor consideration and 14 is for first- and second-nearest-neighbor considerations.

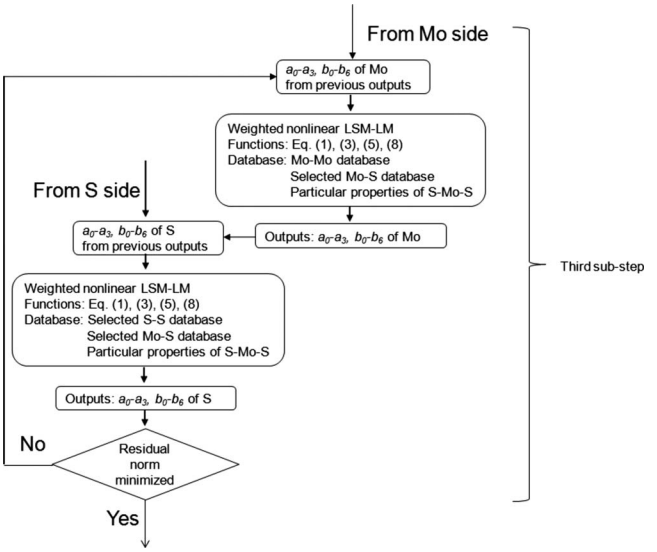

FIG. 4. Flow chart of third substep of parametrization of the many-body parameters.

Mo are regarded as known when we fit the many-body parameters for S. The iteration stops when the return residual norm is minimized. The final results of many-body parameters fitting are given in detail in Sec. II F.

In summary, the fitting scheme used here is optimized by a systematic consideration of the selection of appropriate initial guesses, the choice and the weighing of the parameters in the training databases, and functional forms of the terms in the potential.

The process outlined here is quite general and can be customized to optimize different training parameter sets and be used to fit different empirical potentials.

C. Pairwise parameters for Mo

So as to explore as wide a range of bond lengths and bond angles as possible, the fitting database for Mo systems consists of the Mo dimer, Mo trimer, two-dimensional triangle (tri), hexagonal (hex), and square (squ) lattices, and three-dimensional simple cubic (sc), diamond (dia), bcc, and fcc crystals. The structural information and properties calculated by DFT are listed in Table I, where the first-neighbor interactions only are assumed in calculating the bond energy and bond stiffness.

Since the dimer has only one neighbor, it has no many-body interactions. Thus both G and P in Eq. (2) are zero and the bond order of the dimer is unity. The 2D square and 3D diamond structures both have four first neighbors. The difference of bond properties between these two structures is attributable to the different angle distributions, as well as the different bond lengths. The square structure has two 90° and

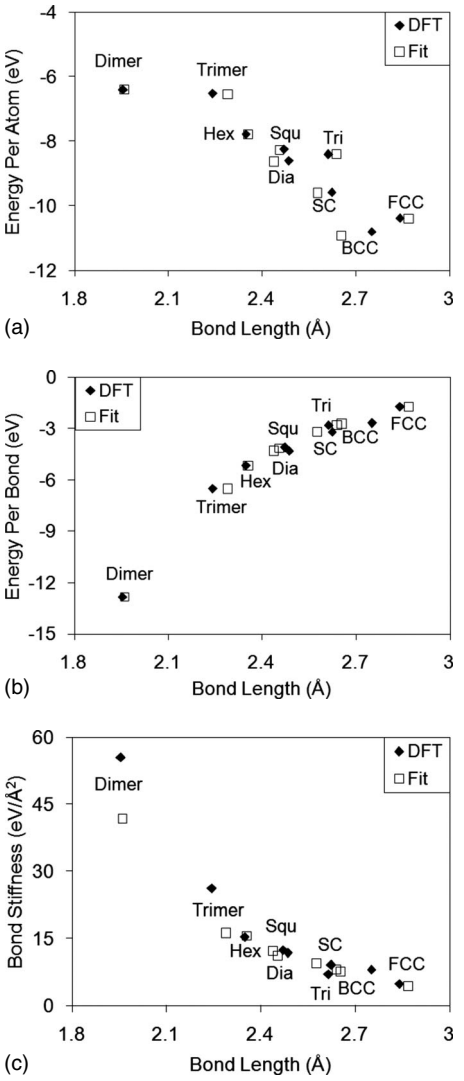

FIG. 5. Plots of the pair term properties of Mo using the parameters in Table II. Top: energy per atom vs bond length, middle: energy per bond vs bond length, and bottom: bond stiffness vs bond length.

one 180° bond angles per atom, whereas diamond has three 109° bond angles. For the same reason, the bond properties are different in the triangular structure (with the angle distribution of two 60°, two 120°, and one 180°) and simple cubic structures (with the angle distribution of four 90° and one 180°). Since the bond-order term is dependent on both the angle distribution and the coordination numbers, each structure has a unique bond-order value. As discussed in Sec. II B, the bond stiffness of the dimer and trimer and the bond properties of the bcc structure excluded in the pairwise parameter fitting. Following the fitting scheme in Fig. 2, the resulting pairwise parameters for Mo bonds are given in Table II. The selection of the cutoff radii in Eq. (5) for Mo

TABLE II. Parameters for Mo-Mo pair terms.

Q=3.41912939005919	A=179.008013654688	B=716.946492819159
α=1.0750071299934	β=1.16100322369589	$R^{\min}$=3.5 Å, $R^{\max}$=3.8 Å

TABLE III. DFT calculated database used in fitting scheme for S-S bonds.

Structures	Coordination number	Bond length (Å)	Energy per atom (eV)	Energy per bond (eV)	Bond stiffness (eV/Å^2)
Dimer	1	1.91	−3.28	−6.55	19.68
Trimer	2	2.03	−3.86	−3.86	11.56
Cyclo-octasulfur	2	2.04	−4.06	−4.06	11.42
Hexagonal	3	2.32	−3.30	−2.20	7.67
Square	4	2.38	−3.62	−1.81	5.63
Diamond	4	2.51	−3.13	−1.56	4.87
Triangle	6	2.54	−3.09	−1.03	3.50
sc	6	2.59	−3.51	−1.17	3.67
fcc	12	2.83	−2.84	−0.47	1.64
bcc	8	2.75[a]	−3.01[a]	−0.75[a]	2.35[a]

[a]Not used in the fitting process of pairwise parameters.

bonds is also listed since they are associated with the pairwise parameters.

Figure 5 compares the energy per atom (atomization energy), energy per bond (within the nearest-neighbor shell), and bond stiffness as a function of equilibrium bond distances in different structures as calculated from DFT and from the fitted potential (Fit). As the number of neighbors in the different structures increases (see Table I), the strong electron-electron repulsion increases the equilibrium bond length (Fig. 5); as a result, the energy per bond (bond energy) and bond stiffness decrease as indicated in the middle and bottom plots in Fig. 5. The only exception is the bond stiffness of bcc (8.0 eV/Å^2), which is larger than that in the lower coordinated triangle structure (6.9 eV/Å^2), an anomaly that is attributable to the first-neighbor approximation, in which all the interactions are ascribed to the first-nearest-neighbor bonds only. Thus the calculated bond energy and bond stiffness are larger than they should be. The overestimation is much greater in the bcc crystal than in the rest of the structures since the second-neighbor interactions within the bcc structure contribute more to the bonding than they do in other structures. To quantify the quality of the fit, the normalized root-mean-square deviation (NRMSD) of each bond property in Fig. 5 has been calculated with Eq. (10),

$$\mathrm{NRMSD} = \frac{\mathrm{RMSD}}{x_{\max} - x_{\min}} = \frac{\sqrt{\sum_i^n (\hat{x}_i - x_i)^2/n}}{x_{\max} - x_{\min}}, \qquad (10)$$

where $\hat{x}_i$ is the predictor value (open squares in Fig. 5) and x_i is the corresponding response value (solid diamonds in Fig. 5). The $x_{\max}$ and $x_{\min}$ are the maximum and minimum values of the response database, respectively. Each difference between the predictor and response values, i.e., $\hat{x}_i - x_i$, is taken to be the residual. Lower values of NRMSD correspond to more accurate fits. The NRMSDs for the energy per atom, energy per bond, bond length, and bond stiffness in Fig. 5 are 0.1%, 1.1%, 5.0%, and 11.1%, respectively. The relatively large deviation for bond stiffness is primarily due to the big residuals of the bond stiffness for dimer and trimer structures (13.7 and 9.8 eV/Å^2), which is not a concern of this study. In general, the fitting results of bond energy, atomization energy, equilibrium bond length, and bond stiffness are in good agreement with the calculated DFT database. It is thus evident that this formalism is capable of describing the bonding properties of Mo structures using a single set of parameters over a large range of interatomic distances and a variety of structures, including molecules, 2D lattice, and 3D crystals.

D. Pairwise parameters for S

In parametrizing the pairwise interactions for S, we have also included a variety of different bonding environments. The DFT results are given in Table III. As is well known, the stable structure of S at 300 K and 1 atm is the cyclo-octasulfur molecule, which is an eight-membered ring. The same fitting scheme that was used for the Mo was used in this case, and the resulting parameters are given in Table IV, while the fits to the DFT results are given in Fig. 6. The NRMSDs for the energy per atom, bond length, and bond stiffness of S structures are 2.9%, 3.7%, and 2.3%, respectively, which indicate the good agreement between the predictor data and response data calculated by DFT.

E. Pairwise parameters for Mo-S

A similar parametrization algorithm is used for Mo-S binary bonds, where the following structures are constructed:

TABLE IV. Parameters for S-S pair terms.

Q=0.254959104053671	A=1228.43233679426	B=1500.21248794408
α=1.10775022439715	β=1.1267362361032	$R^{\min}$=2.6 Å, $R^{\max}$=2.9 Å

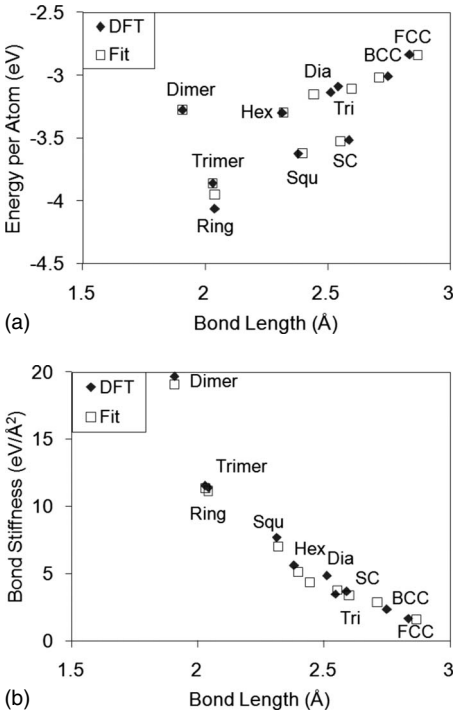

FIG. 6. Plots of the pair term properties of S using the parameters in Table IV. Top: energy per atom vs bond length and bottom: bond stiffness vs bond length.

zinc blend (ZnS), sodium chloride (NaCl), cesium chloride (CsCl), fluorite (CaF_2), quartz (Quartz), cristobalite (Cristo), rutile (TiO_2), and molybdenum disulphide (MoS_2). The Mo-S database calculated from DFT is given in Table V. The pair terms for Mo-S bonding are given in Table VI and the resulting energy per unit and bond stiffness vs bond length is plotted in Fig. 7. The NRMSD for the energy per unit, equilibrium bond length, and bond stiffness for Mo-S bonds are about 1.1%, 15.4%, and 9.2%, respectively.

F. Many-body parameters in the bond-order term

A number of analytic formulas for the bond-order term have been developed. In the traditional Tersoff potential,[24] the bond-order value decays exponentially with the summed value over the bond angles, which implicitly includes the effect of coordination number since the number of bond angles equals the coordination number minus one. The bond-order term in the second-generation REBO (Ref. 22) potential is captured in separate angular and coordination terms. The explicit coordination term $[P(N_i)$ in Eq. (2)] in the REBO potential is numerically fit to a number of cubic spline functions depending on the number of neighbors and the element type of those atoms. This selection of coordination term provides sufficient freedom to capture the chemical reactions that take place in the complex hydrocarbon systems.

In REBO, the angular term, $G[\cos(\theta)]$ in Eq. (2), is selected to be a sixth-order polynomial of the cosine of the angle.[22] This can be regarded as the first seven terms of a Taylor expansion. Since the cosine value varies from −1 to 1 and the inverse factorials in the coefficients decrease rapidly with increasing order, the first seven terms in the expansion are adequate to provide an accurate description of the angular effects. The sixth-order polynomial format also gives a smooth function up to sixth derivatives, which might be required for high-order predictor-corrector algorithms. In REBO, the fitting process for many-body effects starts with finding the specific $G[\cos(\theta)]$ values for specific values of θ in pure systems, tentatively assuming that the coordination effect in the pure systems is zero. Since this assumption is obviously not appropriate, the fitted $G[\cos(\theta)]$ is then modified by another function and the final bond-order values of the binary systems are adjusted by the coordination term in REBO.

Unlike the fitting scheme in REBO, we start the many-body parameter fitting by finding the general trend of the coordination effect, which is of greatest importance. The analytic function of the coordination effect is prescribed ahead of time and takes the form shown in Eq. (3). It is actually constructed based on the plot of the summation of the angular and coordination terms (M_{tot}) vs coordination number (N_i), where M_{tot} equals $(1/b)^2-1$, where b is equal to the bond-order values that are the output parameters of the previous pairwise parameter fitting.

Figure 8 indicates that as the coordination number increases the bond order decreases; thus, the value of M_{tot} also increases. The coordination number has a more significant effect on the bond order for lower coordinated structures than for higher coordinated structures, asymptotically ap-

TABLE V. DFT calculated database used in fitting scheme for Mo-S bonds.

Structures	No. of bonds per unit	Bond length (Å)	Energy per unit (eV)	Energy per bond (eV)	Bond stiffness (eV/Å^2)
Cristo	4	2.23	−19.67	−4.92	16.22
Quartz	4	2.25	−19.72	−4.93	15.84
ZnS	4	2.32	−14.89	−3.72	13.97
TiO_2	6	2.41	−20.09	−3.35	11.63
MoS_2	6	2.44	−21.53	−3.60	13.16
NaCl	6	2.49	−14.47	−2.41	8.51
CaF_2	8	2.55	−19.47	−2.43	8.10
CsCl	8	2.62	−15.15	−1.89	6.25

TABLE VI. Parameters for Mo-S pair terms.

$Q=1.50553783915379$	$A=575.509677721866$	$B=1344.46820036159000$
$\alpha=1.1926790221882$	$\beta=1.26973752204290$	$R^{\min}=2.72$ Å, $R^{\max}=3.02$ Å

proaching a zero value as the number of neighbors approaches infinity. These observations are consistent with the argument of the effect of electron density or bond density on bond order proposed by Abell[23] for Tersoff[24] potentials and by Daw and Baskes for EAM.[32,33,49] If the bond order, b, exponentially decays with the coordination number as described in the Abell and Tersoff forms, the squared bond-order values b^2 should also exponentially decrease as the coordination number increases, but with a different rate. Thus, M_{tot}, which is defined as $(1/b)^2-1$, can be mathematically expressed as Eq. (7). The fitted M_{tot} values are indicated by open squares in Fig. 8. The good agreement between the calculated and fitted M_{tot} values validates the appropriateness of the functional form in Eq. (7). The slight difference in M_{tot} for the structures with the same number of neighbors, for example, 2D square and 3D diamond structures, is attributable to the different angular distributions in those structures. If we assume the mean value of $G[\cos(\theta)]$ is a_0, and combine Eqs. (6) and (7), the analytic function of $P(N_i)$ can thereafter be expressed as Eq. (3).

As discussed in Sec. II B, the energy of the stacking fault on basal plane S (0001) in a single S-Mo-S trilayer and the elastic constants c_{11} and c_{33} of a single S-Mo-S trilayer are considered in the third substep of the step of the fitting scheme. As indicated in Fig. 1, each atomic layer in S-Mo-S trilayer is a 2D triangular lattice with one atom at each lattice point. Based on the relative position of the 2D lattice, there are three equivalent arrangements, namely, A, B, and C. If it is assumed that the stacking sequence within a S-Mo-S trilayer is ABA, the stacking fault on basal plane S (0001) results in an ABC stacking. The energy difference between the ABC and ABA stackings is the stacking fault energy in Table VII. The elastic constants c_{11} and c_{33} are obtained by homogeneously shrinking or expanding a single S-Mo-S trilayer and then fitting the resulting energies to Eq. (9), where the thickness of a single S-Mo-S trilayer is assumed to be the spacing between two S atom planes. The calculated results from DFT calculations are listed in Table VII.

Following the overall fitting scheme described in Figs. 3 and 4, the resulting angular and coordination functions of Mo and S atoms are given in Figs. 9 and 10, respectively. The fitting results of the stacking fault energy and elastic properties for single S-Mo-S trilayer are listed in Table VII together with the results of DFT calculations.

The fitting results of the Mo angular term, $G[\cos(\theta_{ijk})]$, are given as the solid and dashed lines in Fig. 9. Since the cutoff radius of Mo-Mo bond is 3.8 Å (Table II), the second nearest neighbors in bcc Mo and MoS_2 structures are considered. With this form of $G[\cos(\theta_{ijk})]$, the energy well at the zero bond angle θ_{ijk}, i.e., $\cos(\theta_{ijk})=1$, will cause the second nearest neighbors to line up with the first nearest neighbors. To avoid this spurious energy well, a second angular function $\gamma[\cos(\theta_{ijk})]$ is introduced and coupled with $G[\cos(\theta_{ijk})]$. The total angular function retains the value, first derivative and second derivative at θ_{ijk} from 60° to 180° (solid line in Fig. 9) and gradually transitions to $\gamma[\cos(\theta_{ijk})]$ at 0° (dotted line in Fig. 9). Thus, the revised angular function $G^{\text{new}}[\cos(\theta_{ijk})]$ for Mo atoms is given by

$$G^{\text{new}}[\cos(\theta_{ijk})] = G[\cos(\theta_{ijk})] + \psi[\cos(\theta_{ijk})]\{\gamma[\cos(\theta_{ijk})] - G[\cos(\theta_{ijk})]\}, \tag{11}$$

where the function $\psi[\cos(\theta_{ijk})]$ is defined as[11]

$$\psi[\cos(\theta_{ijk})] = \begin{cases} 0 & \cos(\theta_{ijk}) < 0.5 \\ [1-\cos(2\pi(\cos(\theta_{ijk})-0.5))]/2 & 0.5 \le \cos(\theta_{ijk}) \le 1. \end{cases} \tag{12}$$

A similar drop at θ_{ijk} from 0° to 60° is observed for the S angular function. With the cutoff radius 2.9 Å for S-S bonds, the interactions of the second nearest neighbors are terminated artificially. Within the first nearest-neighbor distance, the pairwise repulsion in bond jk will be prohibitively high if atom k lines up with bond ij. Thus, a revised angular function is not necessary for S atoms.

The coordination term $P(N_i)$ is plotted on a reverse axis to better display its effects on the bond order or potential energy. The general trend shown in Fig. 10 is quite similar to the embedding function in EAM potential for Mo.[49] This is one illustration of Brenner's observation[31] that the EAM potential formalism is equivalent to the Tersoff potential with a constant $G[\cos(\theta)]$ value. The slope of $P(N_i)$ at large coordination number is close to the mean value of $G[\cos(\theta)]$, which indicates the saturation of bond-order value at large coordination number, as suggested in Abell's original paper.[23]

We believe that the above fitting scheme provides a reasonable approach to distinguish between angular and coordination contributions in neutral systems. The method andanalytic functions provided in this potential is general and can be extrapolated to other systems.

G. Parameters for Lennard-Jones potentials

MoS_2 has a lamellar structure. As indicated in Fig. 1, each MoS_2 unit cell consists of two S-Mo-S trilayers and the S-Mo-S trilayers are bonded to each other by vdW attraction between S atoms. The vdW interaction in this potential is described by the well-known Lennard-Jones[35,36] form,

$$E_{LJ}(r) = 4\varepsilon\left[\left(\frac{\sigma}{r}\right)^{12} - \left(\frac{\sigma}{r}\right)^{6}\right], \tag{13}$$

where r is interatomic distance and ϵ and σ are parameters. For nearest-neighbor interactions, the equilibrium Lennard-Jones spacing r_0 is related to σ as $r_0^6=2\sigma^6$. Based on Fig. 1, the distance between two adjacent S atoms from two trilayers is 3.5 Å. Thus r_0 is set to 3.5 Å, i.e., σ is 3.13 Å. Assuming the vdW interactions from Mo atoms are negligible, the elastic constant c_{33} of MoS_2 unit cell is a result of a serial alternative connection of two contributions, one from a single S-Mo-S trilayer and the other from vdW interactions of S atoms. Since each MoS_2 unit cell contains two S-Mo-S trilayers and two vdW springs, the c_{33} for the MoS_2 unit cell can be theoretically expressed as $c_{33}=k_1k_2/2(k_1+k_2)$, where k_1 is the spring constant for a single S-Mo-S trilayer and k_2 is the spring constant for the vdW interaction of S atoms. The experimental value of c_{33} for MoS_2 is 52 GPa and the calculated c_{33} for a single S-Mo-S trilayer (k_1) is 493 GPa (Table VII). The elastic constant for vdW interaction (k_2) is therefore 131 GPa.

A system in which the relative positions of atoms within the S-Mo-S trilayers are fixed and only the spacing between two adjacent trilayers is allowed to change is generated to calculate the c_{33} of one MoS_2 unit. The c_{33} of this system is obtained by calculating the energy vs lattice parameter c of the system. We vary the parameter ϵ in Eq. (13) until the resulting c_{33} is 131 GPa. The parameters for the Lennard-Jones potential for S are given in Table VIII.

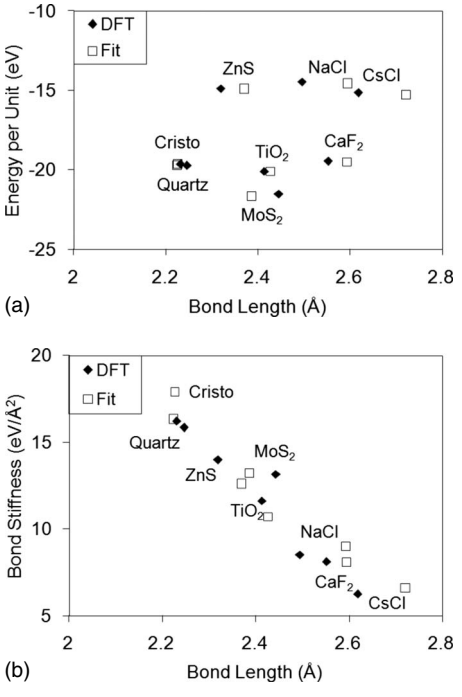

FIG. 7. Plots of the pair term properties of Mo-S using the parameters in Table VI. Top: energy per unit vs bond length and bottom: bond stiffness vs bond length.

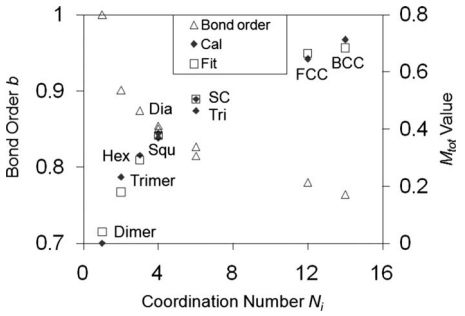

FIG. 8. The bond order (b) varies as a function of the coordination numbers in different Mo structures. Plotted is the summation of the angular and coordination terms (M_{tot}) vs coordination number, where M_{tot} equals $(1/b)^2-1$. The solid diamonds (Cal) are M_{tot} values calculated from discrete bond-order values obtained from pairwise parametrization process, while the open squares (Fit) are fitted values of M_{tot} to Eq. (7).

H. Predicted structural and mechanical properties of Mo and MoS_2

Using the newly developed many-body Mo-S potential, the calculated structural and mechanical properties of Mo and MoS_2 together with experimental (Expt.) values and DFT calculation results are listed in Tables IX and X, respectively.

The lattice parameter and bulk modulus of bcc Mo in Table IX are two of the 27 data points in Table I. However, the c_{11} and c_{12} values for Mo bcc phase were not part of the fitting database. Since the bcc structure is cubic, the bulk modulus B is theoretically related to elastic constants according to $B=(c_{11}+2c_{12})/3$ in an isotropic system. Based on this relation, the values of c_{11} and B calculated by this potential are used to give the value of $c_{12}=306$ GPa.

In Table X, the lattice parameter c and elastic constant c_{33} of MoS_2 are optimized by fitting the Lennard-Jones potential. It is, thus, not surprising that this potential gives a perfect fit to the experimental values. The rest of the properties (lattice parameter a, bulk modulus, and elastic constant c_{11}) of MoS_2 are also part of the fitting database. The fitting scheme used in this study, however, is an overall consideration of many properties listed in Table I, III, V, and VII, not particularly focused on lattice parameter a, bulk modulus, and elastic constant c_{11} of MoS_2. After the compromise made

TABLE VII. Some properties of S-Mo-S single trilayer in MoS_2.

Method	Stacking fault (eV/MoS_2 f.u.)	c_{11} (GPa)	c_{33} (GPa)
DFT	0.37	528	500
Fitted Result	0.44	493	511

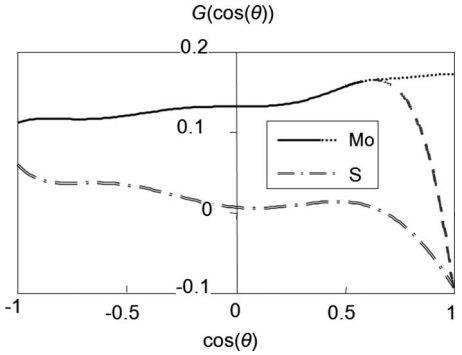

FIG. 9. $G[\cos(\theta)]$ in Eq. (8) vs $\cos(\theta)$ for both Mo and S atoms. The solid and dashed lines are unconstrained fits results of Mo angular term. To avoid the spurious drop as $\cos(\theta)\rightarrow 1$, $G[\cos(\theta)]$ of Mo is adjusted to solid and dotted lines.

in neglecting the effect of charge, this potential fits the training database and nonfitted parameters quite well.

I. Summary

Building upon the proven framework of the Abell,[23] Tersoff,[24–27] and REBO (Refs. 21 and 22) potentials and our successful experience in potential development,[29,30,34] we have extended the REBO potential to Mo-S systems, especially MoS_2. An analytic function is introduced to the bond-order term to characterize the effects of the coordination number on the binding energy. No atomic charges or Coulombic interactions have been included in this Mo-S potential. In addition, the Lennard-Jones potential has been implemented to properly describe vdW interactions between trilayers in MoS_2.

Within the formalism framework of this Mo-S potential, the parametrization procedure is similar to the fitting scheme used in Tersoff's[24–27] and Brenner's[21,22] papers but has been optimized by a systematic consideration of the four key factors that are involved in a weighted nonlinear least-squares fitting.

Followed the improved fitting scheme, this newly developed many-body potential is capable of predicting reasonably good results in energetic, structural properties of pure Mo systems, S molecules, and selected binary systems. More importantly, this potential has successfully reproduced the structural and elastic properties of MoS_2, which is the major interest of this study.

III. CASE STUDY: TRIBOLOGY OF NANOMOLYBDDENUM DISULPHIDE

MoS_2 is the most widely used solid lubricant in aerospace applications. Results from macroscopic studies of MoS_2 have

TABLE VIII. Parameters in Lennard-Jones potential.

	σ (Å)	ϵ (eV)
S-S	3.13	0.00693

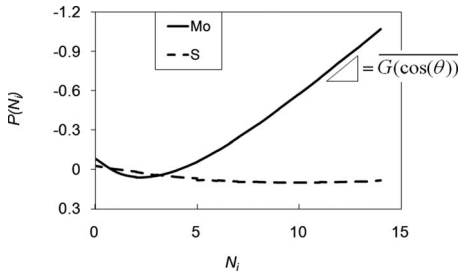

FIG. 10. $P(N_i)$ in Eq. (3) vs coordination number N_i for both Mo and S atoms. The slope at large coordination number values is close to the mean value of $G[\cos(\theta)]$, which indicates the saturation of bond-order value when the coordination number approaches large values (Ref. 23).

contributed much to the phenomenological understanding of its tribology.[51–53] However, the macroscopic studies of interactions between two sliding surfaces are influenced by complex factors, including surface topology, which have precluded the development of an atomic understanding of the friction and adhesion.[51–53] Recently, Liang *et al.*[10] calculated the static energy surface using DFT calculations to analyze the sliding MoS_2/MoS_2 interface. Limited by the computational capacity of first-principles methods, the system in that study consisted of 96 atoms and only considered purely static effects.

To more realistically analyze frictional sliding, a supercell with dimensions of $17.4\times 18.9\times 6.2$ nm^3 (Fig. 11) is considered for our molecular dynamic (MD) simulation of sliding using the MD code that was originally written by Brenner.[21] The system consists of a small S-Mo-S single trilayer flake of 551 atoms sliding over an extended S-Mo-S substrate of 11 520 atoms. Periodic boundary conditions are applied within the plane of the substrate (the X, Y plane). To avoid interactions between images along the Z direction, a 5-nm-thick vacuum is added above the flake in this direction. The load is simulated by manually displacing the S-Mo-S flake downward toward the substrate in the negative Z direction. The displaced system is then equilibrated with the atoms in the top layer of the flake and the bottom layer of the substrate being fixed. The resulting force on the top and bottom layers is about 600 nN, i.e., about 2 GPa. The compressed relaxed system is then used to simulate the sliding of the small flake over the extended S-Mo-S surface. As indicated in Fig. 11, the top S layer of the flake is set to be rigid but is moved manually at a constant rate of 1 m/s in the Y direction. The bottom S layer of the substrate is fixed. A Langevin[54] thermostat is applied to the two sides of the sub-

TABLE IX. Structural and mechanical properties of Mo.

Mo	a (Å)	B (GPa)	c_{11} (GPa)	c_{12} (GPa)
Expt.[a]	3.15	230	450	173
DFT[a]	3.18	266	444	176
This potential	3.15	239	339	306[b]

[a]Reference 50.
[b]Calculated value based on $B=(c_{11}+2c_{12})/3$.

TABLE X. Structural and mechanical properties of MoS_2.

MoS_2	a (Å)	c (Å)	B (GPa)	c_{11} (GPa)	c_{33} (GPa)
Exp.[a]	3.16	12.29	76	238	52
DFT[a,b]	3.10	12.47	68	237	41
This potential	3.16	12.29	75	242	52

[a]Reference 19.
[b]The mean values from the literature.

strate such that temperature of the system equilibrates to ~100 K. This thermostat configuration is appropriate, as thermal transport occurs most strongly in MoS_2 within individual trilayers rather than between trilayers. The simulation lasts a total of 5×10^6 MD steps, and the time step to 0.6 fs.

We track the output structure every 10 000 steps, i.e., 6 ps or 0.006 nm of sliding. The displacements of the output structure with respect to the starting structure in the X, Y, and Z directions of atoms at the bottom layer of the flake are plotted in Fig. 12(a). At the same time, the lateral force (along the sliding direction or the Y axis) and the load (normal to the sliding direction or the Z axis) on the rigid moving atoms (top S layer of the flake) and the fixed atoms (bottom S layer of the substrate) are also calculated. The overall forces are calculated by averaging the lateral force and load from the top layer and the bottom layers. The averaged lateral force, load, and the ratio between them are plotted in Fig. 12(b).

The MoS_2 substrate provides a periodic 2D potential surface, qualitatively identical to the static energy surface previously determined in our earlier DFT calculations (see Fig. 6 in Ref. 10). However, our empirical potential cannot quantitatively reproduce the height of the energy barriers. In particular, while the energy barrier to sliding calculated by DFT is ~0.03 eV/atom, the potential gives a value of only 0.003 eV/atom. Thus while it can be expected to reproduce the correct dynamic path during friction, the MD simulations can be expected to yield significantly lower friction coefficients. This limitation in the fidelity of the potential is not unexpected since the REBO as applied to graphite yields similarly lower potential barrier than predicted by DFT.

While the flake is dragged at 1 m/s along the Y axis over the MoS_2 potential surface, the Y displacement [Y disp in Fig. 12(a)] of the bottom layer of S in the flake increases linearly, but with slight waviness, indicative of "stick-slip" phenomena. The X displacement in Fig. 12(a) suggests that S atoms at the top of the sliding interface periodically move about 0.04 nm to the right and return to the original X position. The zigzag route of atoms at the interface is completely consistent with the predicted sliding pathway (path I in Fig. 6 in Ref. 10) from DFT calculations. Comparing Fig. 6 in Ref. 10 with the Z displacement and the load curve in Fig. 12, the load (along Z direction), as well as the displacement in Z direction, has an instant response to the potential surface. However, the lateral force is unable to follow the potential surface adiabatically, as indicated in dashed line L in Fig. 12(b). The ratio of the lateral force to load ratio varies between −0.8 and 0.9 during sliding. A 50-period moving average of the ratio is also plotted in Fig. 12(b). The moving average of the $F_{//}$/load ratio fluctuates from −0.2 to 0.3 with the mean value of 0.17, which is consistent with the low

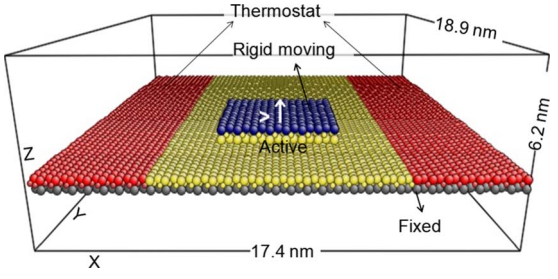

FIG. 11. (Color online) System configuration for friction study consists of a small flake of MoS_2 sliding over an extended MoS_2 surface.

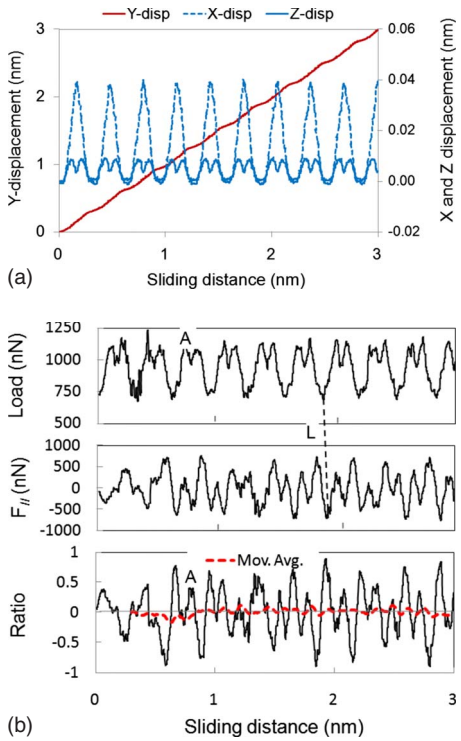

FIG. 12. (Color online) (a) Displacement (with respect to the relaxed system) of atoms at the interface in X (X disp), Y (Y disp), and Z (Z disp) directions; (b) load, lateral force ($F_{//}$), and $F_{//}$/load ratio vs sliding distance. Red dotted line (Mov. Avg.) is the 50-period moving average of the ratio.

values of friction determined experimentally for MoS_2. At position A, the calculated ratio in this study is about 0.42, which is significantly lower than the value of 1.38 determined from the static DFT energy surface. As argued in Ref. 10, the static energy surface calculation is a significant oversimplification of the experimental situation because, in a dynamic sliding process, not all the atoms settle fully into their local minima.

In summary, this newly developed Mo-S potential can be readily applied to examine tribology in MoS_2 systems with MD simulations and has the potential to provide powerful insights of the tribological properties of this material.

IV. CONCLUSIONS

The paper introduces a many-body empirical potential for Mo-S systems using the master formula that underlie the Abell, Tersoff, and REBO potentials. A coordination function inside the bond-order term is constructed based on the general trend of bond-order values over the coordination number in different structures, which in turn reflects the coordination contribution to the binding energy properly. Following the same parametrization sequence in the Tersoff and REBO potentials, we have optimized the fitting scheme by a systematic consideration of the four key factors that are involved in the fitting. The resulting potential yields good agreement with the structural and mechanical properties of Mo and MoS_2. Both the fitting scheme and analytic functions used in this potential are general and can be customized for the specific interests of the study of other systems.

A case study of sliding a MoS_2 flake on a periodic MoS_2 surface is carried out to test the validity of the newly developed potential. The results from this case study are consistent with DFT calculations that are used to simulate the static potential surface of a similar sliding process. With those observations during the sliding, we therefore believe that the newly developed Mo-S potential is capable of capturing the fundamental physical processes associated with sliding. A systematic study of tribological properties of MoS_2 using this potential is ongoing.

ACKNOWLEDGMENTS

The authors are very grateful to W. Gregory Sawyer and Scott Perry for many useful discussions. The authors gratefully acknowledge the support of an AFOSR-MURI under Grant No. FA9550-04-1-0367 and the High-Performance Computing Center, University of Florida for providing computational resources and support.

*Corresponding author; ssinn@mse.ufl.edu

[1] P. Raybaud, J. Hafner, G. Kresse, and H. Toulhoat, Surf. Sci. **407**, 237 (1998).
[2] J. M. Martin, C. Donnet, T. Le Mogne, and T. Epicier, Phys. Rev. B **48**, 10583 (1993).
[3] H. Schweiger, P. Raybaud, G. Kresse, and H. Toulhoat, J. Catal. **207**, 76 (2002).
[4] S. Cristol, J. F. Paul, E. Payen, D. Bougeard, S. Clemendot, and F. Hutschka, J. Phys. Chem. B **106**, 5659 (2002).
[5] P. Raybaud, J. Hafner, G. Kresse, S. Kasztelan, and H. Toulhoat, J. Catal. **190**, 128 (2000).
[6] O. El Beqqali, I. Zorkani, F. Rogemond, H. Chermette, R. Ben Chaabane, M. Gamoudi, and G. Guillaud, Synth. Met. **90**, 165 (1997).
[7] K. Hermann, M. Witko, and A. Michalak, Catal. Today **50**, 567 (1999).
[8] J. A. Spirko, M. L. Neiman, A. M. Oelker, and K. Klier, Surf. Sci. **542**, 192 (2003).
[9] J. A. Spirko, M. L. Neiman, A. M. Oelker, and K. Klier, Surf. Sci. **572**, 191 (2004).
[10] T. Liang, W. G. Sawyer, S. S. Perry, S. B. Sinnott, and S. R. Phillpot, Phys. Rev. B **77**, 104105 (2008).
[11] W. Zhong and D. Tomanek, Phys. Rev. Lett. **64**, 3054 (1990).
[12] H. Chermette, F. Rogemond, O. El Beqqali, J. F. Paul, C. Donnet, J. M. Martin, and T. Le Mogne, Surf. Sci. **472**, 97 (2001).
[13] G. S. Smith, N. A. Modine, U. V. Waghmare, and E. Kaxiras, J. Comput.-Aided Mater. Des. **5**, 61 (1998).
[14] B. Hinnemann, J. K. Norskov, and H. Topsoe, J. Phys. Chem. B **109**, 2245 (2005).
[15] J. D. Fuhr, J. O. Sofo, and A. Saul, Phys. Rev. B **60**, 8343 (1999).
[16] P. Raybaud, J. Hafner, G. Kresse, and H. Toulhoat, Phys. Rev. Lett. **80**, 1481 (1998).
[17] T. Todorova, V. Alexiev, R. Prins, and T. Weber, Phys. Chem. Chem. Phys. **6**, 3023 (2004).
[18] A. Travert, C. Dujardin, F. Mauge, S. Cristol, J. F. Paul, E. Payen, and D. Bougeard, Catal. Today **70**, 255 (2001).
[19] V. Alexiev, R. Prins, and T. Weber, Phys. Chem. Chem. Phys. **2**, 1815 (2000).
[20] V. Alexiev, R. Prins, and T. Weber, Phys. Chem. Chem. Phys. **3**, 5326 (2001).
[21] D. W. Brenner, Phys. Rev. B **42**, 9458 (1990).
[22] D. W. Brenner, O. A. Shenderova, J. A. Harrison, S. J. Stuart, B. Ni, and S. B. Sinnott, J. Phys.: Condens. Matter **14**, 783 (2002).
[23] G. C. Abell, Phys. Rev. B **31**, 6184 (1985).
[24] J. Tersoff, Phys. Rev. Lett. **56**, 632 (1986).
[25] J. Tersoff, Phys. Rev. Lett. **61**, 2879 (1988).
[26] J. Tersoff, Phys. Rev. B **37**, 6991 (1988).
[27] J. Tersoff, Phys. Rev. B **39**, 5566 (1989).
[28] S. J. Stuart, A. B. Tutein, and J. A. Harrison, J. Chem. Phys. **112**, 6472 (2000).
[29] I. Jang and S. B. Sinnott, J. Phys. Chem. B **108**, 18993 (2004).
[30] B. Ni, K.-h. Lee, and S. B. Sinnott, J. Phys.: Condens. Matter **16**, 7261 (2004).
[31] D. W. Brenner, Phys. Rev. Lett. **63**, 1022 (1989).
[32] M. S. Daw and M. I. Baskes, Phys. Rev. Lett. **50**, 1285 (1983).
[33] M. S. Daw and M. I. Baskes, Phys. Rev. B **29**, 6443 (1984).
[34] J. Yu, S. B. Sinnott, and S. R. Phillpot, Philos. Mag. Lett. **89**, 136 (2009).
[35] J. E. Jones, Proc. R. Soc. London, Ser. A **106**, 441 (1924).

[36] J. E. Jones, Proc. R. Soc. London, Ser. A **106**, 463 (1924).
[37] H. Rydberg, M. Dion, N. Jacobson, E. Schröder, P. Hyldgaard, S. I. Simak, D. C. Langreth, and B. I. Lundqvist, Phys. Rev. Lett. **91**, 126402 (2003).
[38] H. Rydberg, B. I. Lundqvist, D. C. Langreth, and M. Dion, Phys. Rev. B **62**, 6997 (2000).
[39] http://cms.mpi.univie.ac.at/vasp/
[40] G. Kresse and J. Hafner, Phys. Rev. B **47**, 558 (1993).
[41] G. Kresse and J. Hafner, Phys. Rev. B **49**, 14251 (1994).
[42] G. Kresse and J. Furthmüller, Comput. Mater. Sci. **6**, 15 (1996).
[43] G. Kresse and J. Furthmüller, Phys. Rev. B **54**, 11169 (1996).
[44] J. P. Perdew and A. Zunger, Phys. Rev. B **23**, 5048 (1981).
[45] J. P. Perdew, J. A. Chevary, S. H. Vosko, K. A. Jackson, M. R. Pederson, D. J. Singh, and C. Fiolhais, Phys. Rev. B **46**, 6671 (1992).
[46] J. P. Perdew and Y. Wang, Phys. Rev. B **45**, 13244 (1992).
[47] K. Levenberg, Q. Appl. Math. **2**, 164 (1944).
[48] D. Marquardt, SIAM J. Appl. Math. **11**, 431 (1963).
[49] M. I. Baskes, Mater. Sci. Eng., A **261**, 165 (1999).
[50] S. L. Frederiksen, K. W. Jacobsen, K. S. Brown, and J. P. Sethna, Phys. Rev. Lett. **93**, 165501 (2004).
[51] E. Gnecco, R. Bennewitz, and E. Meyer, Phys. Rev. Lett. **88**, 215501 (2002).
[52] J. A. Harrison, S. J. Stuart, and D. W. Brenner, in *Handbook of Micro/Nanotribology*, edited by B. Bhushan (CRC, Boca Raton, 1999), p. 525.
[53] S. B. Sinnott, S.-J. Heo, D. W. Brenner, and J. A. Harrison, in *Springer Handbook on Nanotechnology*, edited by B. Bhushan (Springer-Verlag, Heidelberg, 2007), p. 1051.
[54] S. A. Adelman and J. D. Doll, J. Chem. Phys. **64**, 2375 (1976).